Hydrogen Passivated VZn -GaZn Complexes as Major Defects in Ga-doped ZnO Nanowires Evidenced by X-Ray Linear Dichroism and Density Functional Theory

Eirini Sarigiannidou, Pierre Gaffuri, Fabrice Wilhelm, Joseph Kioseoglou, Andrei Rogalev, Efstratios Nikidis, Estelle Appert, Vincent Consonni

Hydrogen Passivated V_{Zn} – Ga_{Zn} Complexes as Major Defects in Ga-doped ZnO Nanowires Evidenced by X-Ray Linear Dichroism and Density Functional Theory

Eirini Sarigiannidou,[1*] Pierre Gaffuri,[1] Fabrice Wilhelm,[2] Joseph Kioseoglou,[3] Andrei Rogalev,[2] Efstratios Nikidis[3] Estelle Appert,[1] and Vincent Consonni.[1]

[1] Université Grenoble Alpes, CNRS, Grenoble INP, LMGP, 38016 Grenoble, France

[2] European Synchrotron Radiation Facility (ESRF), 71 avenue des Martyrs, 38043 Grenoble, France

[3] Physics Department, Aristotle University of Thessaloniki, 54124 Thessaloniki, Greece

CORRESPONDING AUTHOR FOOTNOTE:

*E-mail: eirini.sarigiannidou@grenoble-inp.fr

ABSTRACT

The elucidation of the residual and intentional doping processes in ZnO nanowires grown by chemical bath deposition is a major, but still largely unexplored issue despite its primary importance for a large number of nanoscale engineering devices. Here, we investigate the local structural environment around Ga dopants in ZnO nanowires by combining synchrotron radiation-based X-ray linear dichroism with density-functional theory calculations. We show that the family of V_{Zn}-Ga_{Zn}-*n*H defect complexes is predominantly formed and hence that hydrogen acts as an efficient passivating species even for intentional dopants like Ga. The residual and intentional doping processes are found to be highly correlated through significant interplay effects. These findings revisit the nature of intentional dopant-induced defects and defect complexes in ZnO nanowires. They further reveal that hydrogen should be taken into account in unintentionally doped ZnO nanowires grown by chemical bath deposition as major defects, but also in intentionally doped ZnO nanowires through its efficient passivating effect, opening perspectives to more finely control their optical and electrical properties.

KEYWORDS: ZnO nanowires, hydrogen, Ga doping, X-ray Linear Dichroism, density functional theory.

INTRODUCTION

The development of ZnO nanowires (NWs) by chemical bath deposition (CBD) [1,2] has received a great attention over the past decades for a wide variety of engineering devices [3-9]. However, while the structural morphology of ZnO NWs including their shape, verticality, and dimensions (e.g. length, diameter) has been optimized on many types of substrates [10,11], the control over their optical and electrical properties has not been achieved yet. This significantly reduces the performance of devices made of ZnO NWs. In that respect, the residual and intentional doping processes of ZnO NWs grown by CBD along with their possible interaction are still valuable but largely unknown.

Generally, the issue of native defects and hydrogen in ZnO has highly been debated and a couple of consensus has emerged from experimental and theoretical data [12,13]. Zn vacancy (V_{Zn}) has been found to be the dominant negatively charged native defect using positron annihilation experiments [14]. From density-functional theory (DFT) calculations, V_{Zn} is known to exhibit a low formation energy when the Fermi level is close to the conduction band minimum (CBM) and to be the most favorable native point defect specifically under intermediate and oxygen-rich conditions [15]. It acts as a deep acceptor with a –2 charge state [15] and presents a typical emission line around 1.6 eV using optical spectroscopy [16]. In addition to the role of V_{Zn}, hydrogen-related defects including interstitial hydrogen in bond-centered sites (H_{BC}) [17] and substitutional hydrogen on the oxygen sites (H_O) [18] have been shown to be the source of the *n*-type conductivity of ZnO [19], excluding the role of oxygen vacancy (V_O) acting as a deep donor [20]. H_{BC} and H_O with the +1 charge state act as two shallow donors with a very low formation energy, regardless of the Fermi level in the bandgap [17,18]. Moreover, several types of defect complexes related to V_{Zn} and interstitial hydrogen (H_i) [20-22] as well as to substitutional nitrogen on the oxygen sites (N_O) [23-27] have been investigated experimentally and by DFT calculations and in all the cases the charge state is considered from +2 down to –2 due to the implication of V_{Zn}. More recently, it has also been suggested that hydrogen may combine with intentional dopants such as group III-A elements to form more complicated defect complexes [21].

On the basis of that well-established knowledge, the residual and intentional doping processes of ZnO NWs grown by CBD as the currently most important deposition technique are largely unknown and strongly affected by the aqueous medium, which is polar and contains a large amount of hydrogen and nitrogen. On the one hand, a couple of recent reports have shown that hydrogen is massively incorporated into ZnO NWs when grown by CBD through a residual doping process [28,29] and forms a large number of defects including H_{BC} and V_{Zn}-3H complexes [22,27]. On the other hand, following the optimization of the process conditions during the CBD, a number of dopants including Al [30], Ga [31], Cu [32], and Sb [33] has been used to be incorporated into ZnO NWs through an intentional doping process. Among them, Ga acting as

a shallow donor [34] is one of the most investigated dopants in ZnO NWs owing to its high potential in the fields of optoelectronics [31,35-39]. Following both statements, one of the most important and yet open question relies on how the residual and intentional doping processes interact each other and hence affect the local atomic structure around the intentional dopants incorporated into ZnO NWs. This open question is crucial as the local atomic structure governs the electrical activity of intentional dopants and hence the doping efficiency in ZnO NWs, but it has never been explored owing to the inherent experimental limitations.

The accurate and precise determination of the local atomic structure around an intentional dopant is a prerequisite to control the physical properties of ZnO NWs and hence to tune the macroscopic response to different solicitations for engineering devices. X-ray diffraction, X-ray photoelectron spectroscopy, high-resolution transmission electron microscopy, Raman spectroscopy and X-ray absorption spectroscopy (XAS) can provide detailed information on the local electronic and atomic structure. Nevertheless, discriminating the nature of dopant-induced defects that are present in a host lattice still constitutes a challenging task. XAS provides a set of element-specific probes that are suitable for studying thin films and nanomaterials. For example, X-ray absorption near edge structure (XANES) and extended X-ray absorption fine structures (EXAFS) have extensively been used to reveal the presence of cobalt vacancy-related complexes in Co-doped ZnO films [40] or V_{Zn} in Cu-doped ZnO diluted magnetic semiconductor films [41]. However, the sensitivity of those methods rely on the small modifications of the relative intensity of all the spectral features of the XANES measurements or on the complicated data treatment within EXAFS analysis. In contrast, X-ray linear dichroism (XLD) allows to probe the local structural environment and, as a differential spectroscopy method, it is inherently a very sensitive characterization technique. The power of XLD was first demonstrated on Mn-doped GaN films [42] and then on Co-doped ZnO films [43] to quantitatively assess the fraction of the absorbing atomic species incorporated at a specific lattice site in diluted magnetic semiconductors. Until now, a comprehensive investigation of the local atomic structure of Ga-doped ZnO NWs is practically non-existing in the literature despite its primary importance.

In the present work, to establish the correlation between the residual and intentional doping processes, a full description of the local structural environment around Ga dopants in ZnO NWs grown by CBD is studied by XLD measurements recorded at the Zn and Ga K-edges using synchrotron-based X-ray radiation. Structural models of intentional dopant-induced defects and defect complexes in ZnO are investigated by DFT calculations. The resulting relaxed atomic structures are then used as an input data for XANES and XLD simulations and confronted with the recorded experimental XANES and XLD spectra, respectively. We demonstrate that hydrogen passivated $V_{Zn} – Ga_{Zn}$ defect complexes are the predominantly major defects in ZnO NWs grown by CBD. These findings revisit the nature of intentional dopant-induced defects and

defect complexes in ZnO NWs grown by CBD, emphasizing the need for considering hydrogen as an efficient passivating species.

EXPERIMENTAL & THEORETICAL DETAILS

Synthesis method. Ga-doped ZnO NW arrays were grown on (001) silicon (Si) wafers using a two-step chemical synthesis process as described in Ref.[31]. First, a *c*-axis oriented polycrystalline ZnO seed layers was deposited by dip coating. The prepared solution, an equimolar mix of 375 mM of both zinc acetate dihydrate ($Zn(CH_3COO)_2 \cdot 2H2O$, Emsure ACS) and monoethanolamine (MEA, Sigma-Aldrich) in pure ethanol, was heated and stirred 60 °C for 12 h and then remained for 12h more at the room temperature. The xerogel film was formed by dipping the Si wafer in the solution and withdrawn at the speed of 3.3 mm/s in ambient atmosphere with controlled hygrometry measured less than 15%. The xerogel film was annealed in air on a hot plate first at 300 °C for 1 h to evaporate the solvent and organic residues and then at 500 °C for 3 h to achieve its crystallization. Secondly, vertically c-axis oriented Ga doped ZnO NWs were grown by chemical bath deposition (CBD). The ZnO seed layer-coated silicon wafer was immersed face down in a sealed beaker containing an equimolar mix of 30 mM zinc nitrate hexahydrate ($Zn(NO_3)_2 \cdot 6H_2O$, Sigma-Aldrich) and HMTA ($C_6H_{12}N_4$, Sigma-Aldrich) in deionized water, together with 0.75 mM of gallium nitrate hydrate ($Ga(NO_3)_3 \cdot xH_2O$,Sigma-Aldrich). The pH of the solution prior to heating was equal to 10.9 by the addition of 584 mM of ammonia (NH3, VWR Chemicals). The sealed beaker containing the solution was placed in a regular oven heated at 85 °C for 3 h. Both the pH and temperature of the solution were monitored in an in-situ manner to follow their variation as CBD proceeds.

Characterization techniques. The pH and temperature of the solution as CBD proceeds were monitored in an *in situ* manner using an InLab Versatile Pro pH electrode from Mettler Toledo. The morphology and structural properties of ZnO NWs were measured by top-view and cross-sectional view FESEM images using a FEI Quanta 250 field-emission-gun scanning electron microscope. The Ga incorporation into ZnO NW arrays was investigated by EDS analyses and Raman scattering measurements. FESEM-EDS spectra of ZnO NW arrays were collected using a Bruker x-ray detector incorporated into the FEI Quanta 250 FESEM instrument operating at 20 kV. STEM specimens were prepared by scratching the surface of ZnO NW arrays using a diamond tip and spread on a Cu grid. STEM-EDS spectra and maps of single ZnO NWs were recorded with a JEOL SDD Centurio detector incorporated into a JEOL 2100F FESEM instrument operating at 200 kV and having a 0.2 nm resolution in the scanning mode. Raman scattering measurements were performed using a Horiba/Jobin Yvon Labram spectrometer equipped with a liquid-nitrogen-cooled CCD detector. The 488 nm excitation line of an Ar^+ laser was used with a power on the sample surface lower than 10 mW. The laser beam was focused to a spot size of 1 μm^2 using a 50 times long working distance objective. The spectra were calibrated in wavenumber at room temperature by

using a silicon reference sample and considering that the theoretical position of the silicon Raman line is set to 520.7 cm^{-1}.

XANES & XLD measurements. XANES measurements were carried out at the ID12 beamline at the European Synchrotron Radiation Facility (ESRF) in Grenoble (France).[44] The XANES was recorded for two orthogonal linear polarizations. A 0.9 mm thick diamond quarter wave plate was used to flip several times at each energy point the linearly polarized x-rays from vertical to horizontal by converting the incoming circularly polarized x-rays emitted by the second harmonic of the HELIOS-II type HU52 and APPLE-II type HU38 helical undulators at the Zn and Ga K-edge respectively. To reduce the heat load of the first harmonic of the helical undulators, 100 microns Al foil was inserted ahead of the Si(111) double crystal monochromator. The sample was measured at 10°grazing incidence, *i.e.* vertical linear polarization strictly perpendicular to the c-axis direction (the *E*-vector of the light ⊥ to the c axis) of the nanowires whereas the horizontal linear polarization is close to the c-axis direction (*E-vector* //c). For the Zn and Ga K-edges, total fluorescence yield (TFY) was used as detection system. Additionally, the XANES spectrum at the Zn K-edge was also measured with the total electron yield (TEY) and used as reference for correcting the self-absorption effects of the XANES spectra measured in TFY. The XLD was then taken as the direct difference of the normalized XANES with $E \perp c$ and $E // c$. The isotropic XANES was derived from the weighted average of the two spectra, i.e., (2×XANES($E \perp c$)+XANES($E // c$))/3. The XANES and XLD spectra at the Zn and Ga K-edge were simulated using the *ab initio* FDMNES code.[45,46] For both the Zn and Ga K-edge, the calculations were performed using the finite difference method (FDM). Self-consistency and relativistic effects were not included in the calculations since the agreement between the experimental and theoretical XANES and XLD spectra was not improved. As the 3*d* electron shell for the both Zn and Ga is full ($3d^{10}$), quadrupolar transitions were not included. For the FDMNES simulations, we used the relaxed structural models calculated previously from VASP. The convergence of the FDMNES calculations was checked for increasing cluster sizes and only minor evolutions were found for cluster radii above 9.0 Å. The simulated in-plane XANES component is taken as the averaged over the different in-plane axis since the nanowires are randomly oriented in plane. The simulated spectra were convoluted using a step-like energy-dependent broadening. The step-like energy-dependent broadening was centered at ~20 eV above the inflection point of the XANES for both Zn and Ga K-edge. The core-hole lifetime of 1.67 eV for Zn, 1.82 eV for Ga, the experimental energy resolution (1.3 eV) and a thermic disorder using the Debye model to damp the EXAFS part of the XAS spectrum were taken into account for the convolution. The simulated XLD spectra were rescaled by a factor of ~0.6 and the corresponding XANES spectra for both linear polarizations were then recalculated. Using this procedure, a better agreement regarding the spectral shape with the experimental data was reached for both XLD and XANES spectra at the Zn K-edge.

DFT calculations. The investigation of the wurtzite ZnO structure was performed using the VASP code[47,48] with Projector Augmented-Wave potentials (PAW)[49] under the Perdew-Burke-Ernzerh derivation of the Generalized Gradient Approximation (GGA-PBE)[50,51] of the DFT. The reciprocal-space resolution for k-point mesh generation was set by a Monkhorst-Pack mesh of 8x8x6 for the 1x1x1 unit cell, while the k-point mesh is Γ-centered and the cut-off energy is set at 600 eV. For the present study, a 4x4x3 cell consisting of 192 atoms was considered, while convergence with respect to k-point sampling, slab and vacuum thickness was explicitly checked. Extensive tests concluded that smaller cells are insufficient for the structural relaxation and the accurate calculations of the optoelectronic properties of the point defects in ZnO. Reliable optical properties require an accurate determination of the electronic band gap. Hence, the DFT+*U* method was used in order to accurately calculate the electronic and optical properties. The DFT+*U* approach is better at describing systems with localized *d* and *f* electrons. A strong intra-atomic interaction was introduced in a screened manner as an on-site replacement of DFT. In this work, the simplified rotationally-invariant approach to DFT+*U* introduced in Ref.[52] was used. Initially, *U* was incorporated only for the *d* states of Zn and the $U_{d,\mathrm{Zn}}$ was set to 7.5, a parameter that produces good lattice constants and significantly improves the bandgap of ZnO from 0.70 eV to 1.85 eV as reported in Ref.[53]. Nevertheless, it was shown in Ref.[54] that the correct band gap can be obtained, if in addition to the *U* values for the *d* states, *U* values are considered also for the *s* or *p* states. The corresponding *U* values were obtained from Refs.[55,56]: $U_{d,\mathrm{Zn}}$=10.5 eV, and $U_{p,\mathrm{O}}$=7.0 eV. It should be noted that the lattice constants are slightly underestimated. In addition, in order to accurately reproduce the electronic properties of β-Ga_2O_3, the $U_{d,\mathrm{Ga}}$=7.0 eV was used in consistency with our previous studies and the literature.[57]

Mainly in the previous related studies, significantly smaller supercells of 72 atoms [34] and of 96 atoms [21] were used with hybrid functionals. It is well-known that the formation energies are significantly higher using the + *U* method than using the hybrid functionals calculations. This difference is mainly due to the valence band maximum (VBM) position shift on the absolute energy scale. In the + *U* extrapolation approach, it is assumed that the VBM was well described. However, hybrid functionals calculations showed that the VBM shifted down by approximately 1.7 eV compared to GGA calculations [58], likely due to self-interaction corrections to the VB states not considered in the +*U* method [59]. As a result, the VBM has an additional downward shift of about 1.5 eV compared to the +*U* method [59].

In general, in the present study, the calculated heat of formation is much larger than previous calculations due to the GGA+*U* approach that we have implemented. Previous GGA DFT based calculations concluded that the ε(1+/0) transition level of Ga_{Zn} is at 1.5 eV above the VBM, while by the use of different +*U* with respect to ours, the transition level is found at 2.1 eV or by using the extrapolate formula at 3.9 eV [60] from the VBM. The band gap extrapolation formula of A. Janotti *et al.* [15] was

used to extrapolate the band gap following the DFT+*U* approach to the experimentally calculated value of 3.4 eV in ZnO. Following the band gap extrapolation formula, the transition energy levels depend linearly on +*U* as follows:

$$\varepsilon(q/q')=\varepsilon(q/q')^{DFT+U}+\frac{\Delta\varepsilon}{\Delta E_g}(E_g^{\exp}-E_g^{DFT+U}) \quad (1)$$

where $$\frac{\Delta\varepsilon}{\Delta E_g}=\frac{\varepsilon(q/q')^{DFT+U}-\varepsilon(q/q')^{DFT}}{E_g^{DFT+U}-E_g^{DFT}} \quad (2)$$

However, in the present study the DFT+*U* approach calculate the correct experimental band gap energy value (3.4 eV). Hence, our calculated transition energy levels correspond to those found in the literature when using the band gap extrapolation formula of A. Janotti *et al*. [15]. However, by the use of hybrid functionals [34], the ε(1+/0) transition level is found at 3 eV from the VBM, while, in the present study, it is found above the conduction band minimum indicating that Ga_{Zn} acts as shallow donor in agreement with Ref. [60].

RESULTS & DISCUSSION

The addition of $Ga(NO_3)_3$ in the chemical bath is a typical way to intentionally dope ZnO NWs with Ga using CBD. In the high pH region, $Ga(OH)_4^-$ complexes are predominantly formed in the chemical bath and adsorb on the positively-charged nonpolar *m*-plane sidewalls of ZnO NWs following attractive electrostatic forces. The adsorption process is favourable for the incorporation process of Ga dopants into ZnO NWs, but also alter the development of the *m*-plane sidewalls by notably increasing the radial growth. The structural morphology and physicochemical properties of Ga-doped ZnO NWs are presented in **Figure 1**. Ga-doped ZnO NWs are vertically aligned on top of the *c*-axis oriented ZnO seed layer and exhibit a relatively flat faceted hexagonal tip, as seen in **Figure 1a**. They have a mean length and diameter of around 4 µm and 100 nm with an apparent density of around 40 NW/µm^2. By using a $[Ga(NO_3)_3]/[Zn(NO_3)_2]$ ratio of 2.5%, ZnO NWs are significantly doped with Ga, as shown by the Ga K_α line located at 9.25 eV in **Figure 1c**. A high Ga/Zn element ratio of around 1.5 to 2% is measured using the FESEM-EDS analysis. The spatial distribution of Ga dopants in ZnO NWs is further homogeneous, as seen in **Figure 1b**. The incorporation process of Ga is also indicated by the increase in the intensity of the A_1(LO) line at 574 cm^{-1} and by the presence of additional modes (AM_{Ga}) located at 633.5 and 696.1 cm^{-1} as presented in **Figure 1d**.

These particularities are strongly characteristic of the effective doping of ZnO NWs with Ga. Additionally, the crystallinity of Ga-doped ZnO NWs is high as indicated by the intense, narrow E_2^{High} line at around 438 cm^{-1}, and no extended defects are formed following the incorporation process of Ga as shown in the TEM image analysis.

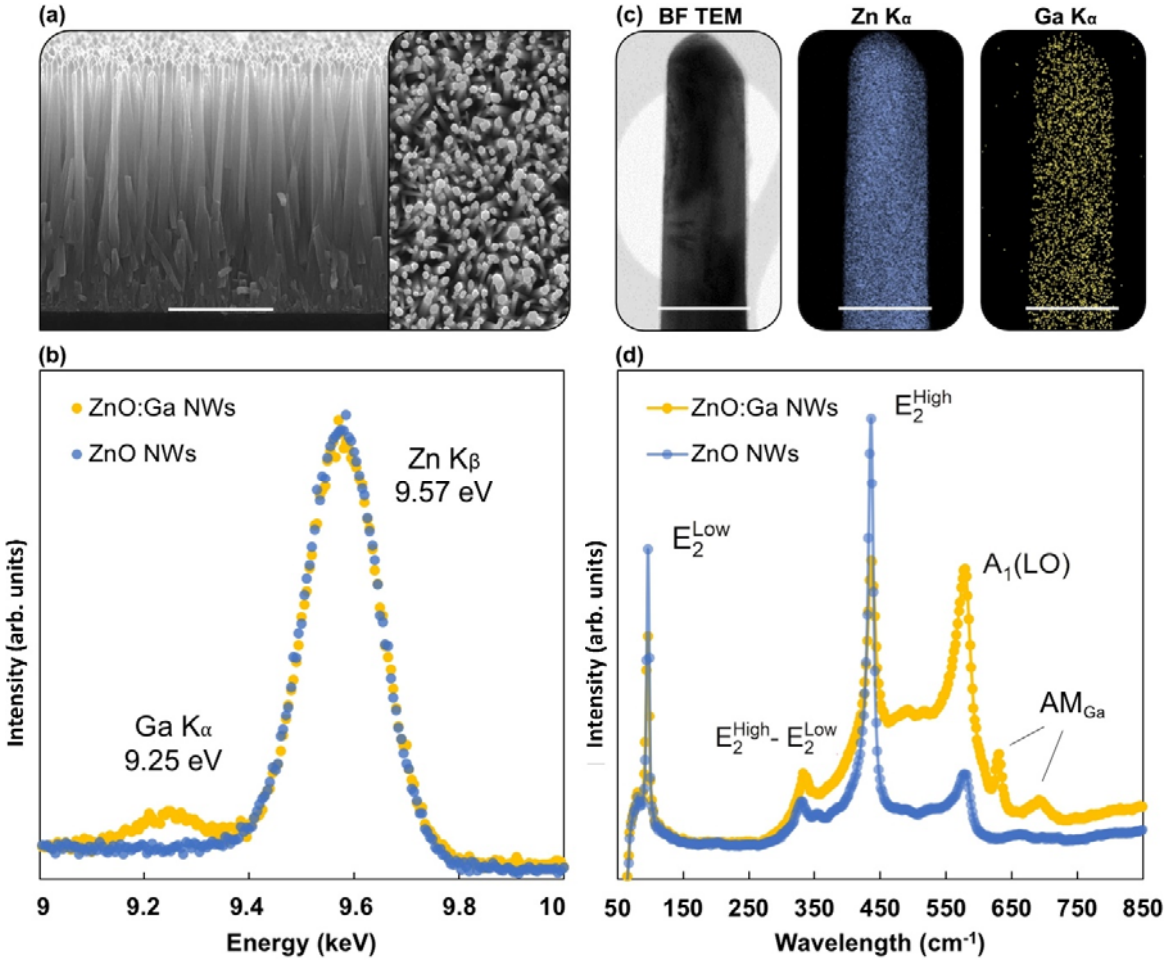

Figure 1. (a) Cross-sectional and top-view FESEM images of Ga-doped ZnO NWs. The scale bar is 2 µm. (b) FESEM-EDS spectra of non-intentionally doped and Ga-doped ZnO NWs. Both spectra were normalized with respect to the Zn K_β line pointed at 9.57 keV. (c) Bright-field TEM image and STEM-EDS elemental maps of Zn and Ga atoms, respectively, collected on a single Ga-doped ZnO NW. The scale bar is 200 nm. (d) Raman scattering spectra of non-intentionally doped and Ga-doped ZnO NWs.

Figure 2a presents the experimental XANES and XLD spectra recorded at the Zn K-edge of Ga-doped ZnO NWs. A clear anisotropy of the XANES spectra is observed and gives rise to a strong XLD signal. The spectral shape of the XLD spectrum is typical for the ZnO wurtzite structure, i.e. a tetrahedral coordination of the Zn^{2+} cation to the surrounding O^{2-} anions. The spectral shape as well as the amplitude of the XLD signal (~71% at the maximum) is identical to ZnO-based samples [43]. This strongly indicates

that the incorporation of Ga dopants with a concentration of around 1.5 to 2% into ZnO NWs hardly disturb the overall bulk wurtzite structure. The open circle lines in **Figure 2a** show the FDMNES simulated Zn K-edge XANES and XLD spectra. They were calculated using a pure ZnO wurtzite structure with the bulk lattice parameters of a = 3.2496 Å and c = 5.2042 Å from Ref. [61] and a dimensionless u-parameter of 0.382 from Ref. [62]. The simulated spectra reproduce very well the experimental one, especially the energy positions and relative amplitudes of the individual peaks in the XANES and thus the XLD spectra. Compared to FDMNES simulations done within the muffin tin approximation (MTA), the rising edge is better reproduced with the FDM except the first small positive peak in the XLD at 9.67 keV.[63] The excellent agreement between the experimental data and simulations done with FDMNES at the Zn K-edge for a pure ZnO wurtzite structure validates the method to be followed when switching to the Ga K-edge. This is in good agreement with the estimation made by comparing the edges jump of Zn and Ga K-edge see Supplementary material in [64].

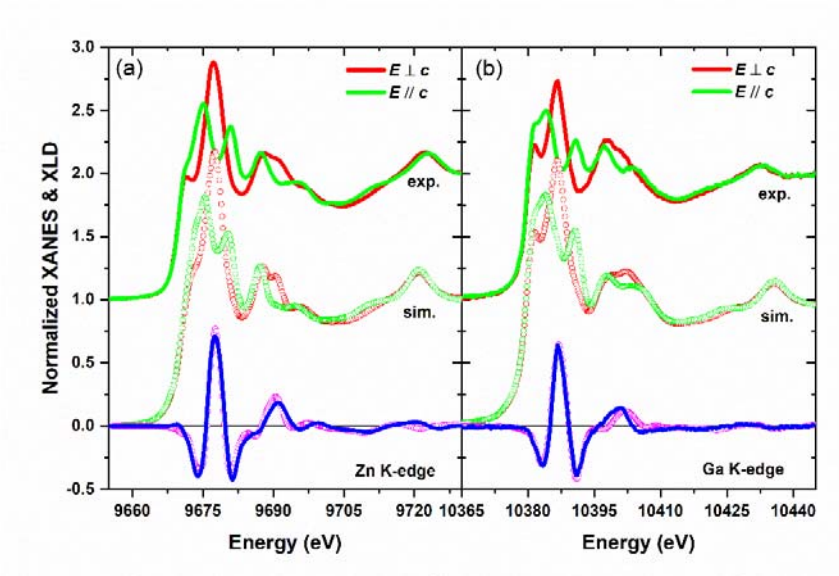

Figure 2. Experimental (solid lines) and simulated (open symbols) normalized XANES spectra recorded with two orthogonal linear polarizations and the corresponding XLD spectra for Ga-doped ZnO NWs at the (a) Zn K-edge and (b) Ga K-edge.

Figure 2b displays the XANES and the respective XLD spectra recorded at the Ga K-edge of Ga-doped ZnO NWs. The spectral shape of both XANES and XLD spectra is nearly similar to the Zn K-edge one, suggesting that Ga dopants substitute for the Zn sites. This can be proven with the help of simulations where Ga dopants can be intentionally placed in different sites within the crystal lattice, i.e. as a substitutional dopant in a Zn site (Ga_{Zn}), as a substitutional dopant in an O site (Ga_O), on an interstitial site (Ga_i), or when

creating defect complexes involving hydrogen atoms. To simulate the XANES and XLD spectra, the relaxed atomic structures determined by DFT calculations were used as an input data.

From **Figure 3**, where the resulted simulated XANES and XLD spectra at the Ga K-edge with a Ga^{2+} electronic state are grouped, it is obvious that the large majority of Ga dopants substitute for the Zn sites since the contribution of the positive peak located at 10380 eV for Ga_i and Ga_O is not observed in the experimental XLD spectrum. Those experimental results are also confirmed from total energy calculations, where Ga_i and Ga_O are energetically unfavorable by more than 6 eV under moderate conditions for the neutral charge state.

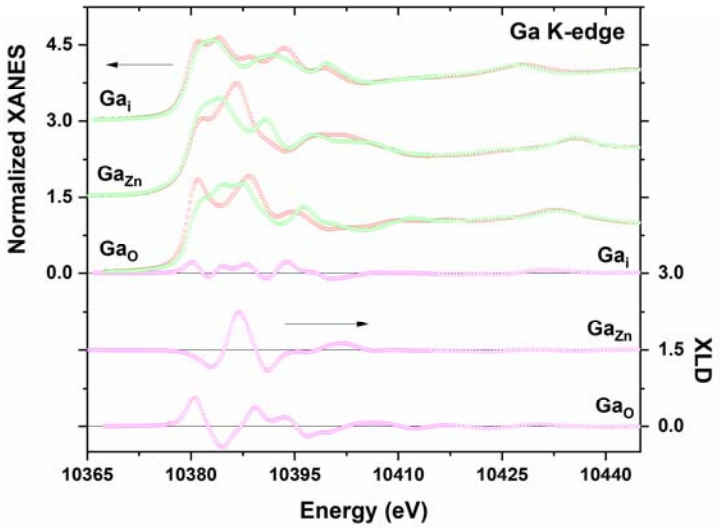

Figure 3. Simulated XANES spectra (left scale) for the two orthogonal linear polarizations at the Ga K-edge and the corresponding XLD spectrum (right scale) for three different positions of Ga in the ZnO lattice structure: Ga in a Zn site (Ga_{Zn}), Ga in an O (Ga_O) site and Ga in an interstitial position (Ga_i). All XANES spectra are normalized to unity and shifted to each other for the sake of clarity.

Knowing that the concentration of V_{Zn} is considerable in ZnO NWs grown by CBD and that they can form defect complexes affecting their electrical conductivity [22], we wanted to investigate and provide a clear experimental evidence about the role of the defect complex V_{Zn}-Ga_{Zn}, i.e. the proximity of Ga_{Zn} with respect to V_{Zn}. Many reports have shown that the XANES signal is sensitive to structural defects [40], but most of them are solely based on the use of only one linear polarization, i.e. only changes in the XANES spectrum but not in the XLD spectrum that is *a fortiori* more sensitive. Moreover, in order to consider the crystallographic characteristics of the wurtzite structure, basal as well as axial, along the *c*-axis, possible atomic positions of the Ga dopants are first studied theoretically by DFT calculations. In particular, two

positions of the Ga_{Zn} on the basal plane V_{Zn}-Ga_{Zn}_B are examined. The first one V_{Zn}-Ga_{Zn}_B1, where the Ga_{Zn} is bonded in the first coordination shell (i.e. first neighbor distance) to an under coordinated O atom due to the V_{Zn}, and the second one V_{Zn}-Ga_{Zn}_B2, where the Ga_{Zn} is bonded in the second coordination shell (i.e. in second neighbor distance) to the under coordinated O atoms. Similarly, concerning the axial direction, the two following cases are considered. The first one V_{Zn}-Ga_{Zn}_A1, where the Ga_{Zn} is bonded in the first coordination shell to an under coordinated O atom above the V_{Zn}, and the second one V_{Zn}-Ga_{Zn}_A2, where the Ga_{Zn} is bonded in the second coordination shell to the under coordinated O atoms, i.e. in a *c*-lattice parameter distance with respect to the V_{Zn}. For each of the four aforementioned cases, five distinct charge cases were considered within the DFT calculations using the VASP code. The neutral, as well as the +2, +1, –1,–2 charge cases are designed by removing 2 or 1 and adding 1 or 2 electrons respectively. Those cases are denoted as e.g. V_{Zn}-Ga_{Zn}_$A1^{+2}$, V_{Zn}-Ga_{Zn}_$A1^{+1}$, V_{Zn}-Ga_{Zn}_$A1^{0}$, V_{Zn}-Ga_{Zn}_$A1^{-1}$, V_{Zn}-Ga_{Zn}_$A1^{-2}$. From DFT calculations, Ga_{Zn} close to the V_{Zn} either in axial A1 or basal B1 positions are found to be energetically favorable (**Figure 4a,b** respectively). Concerning the axial A and basal B possible Ga sites, the axial one (**Figure 4a**) is energetically favorable for neutral and negative charge states while the basal one (**Figure 4b**) is energetically favorable for positive charge states. Regarding the Ga_{Zn} in axial A position, having all hydrogen atoms in basal B positions is the most energetically favorable configuration (3HB,

2HB, HB) (**Figure 4c**), while regarding the Ga_{Zn} in basal B position, sharing hydrogens in basal B and axial A positions is energetically favorable (3H2B1A, 2HBA) (**Figure 4d**).

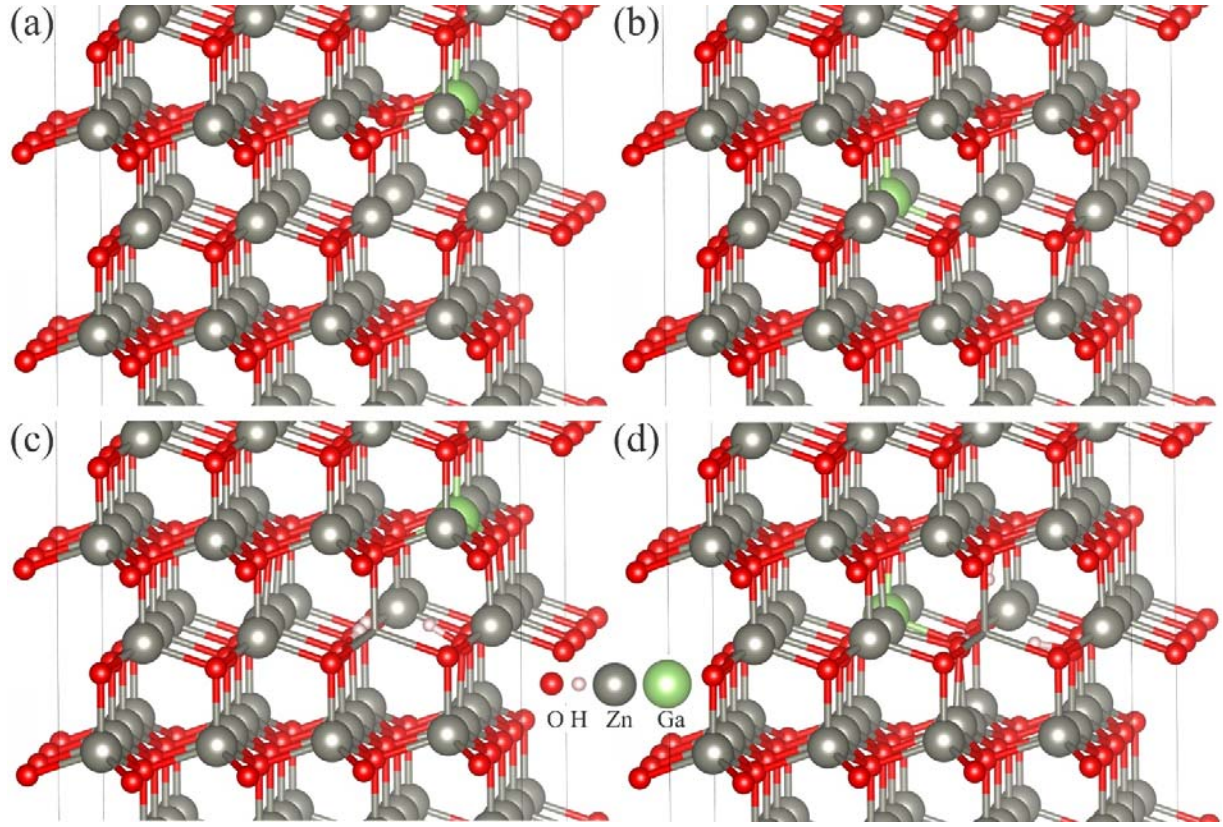

Figure 4. Relaxed structural models for the most stable atomic configurations of V_{Zn}-Ga_{Zn} and V_{Zn}-Ga_{Zn}-*n*H defect complexes. In (a), the axial V_{Zn}-Ga_{Zn}_A1 defect complex is represented. In (b), the basal V_{Zn}-Ga_{Zn}_B1 defect complex is represented. In (c), the $V_{Zn}Ga_{Zn}$_A1_3HB defect complex is represented, where the Ga_{Zn} lies in the axial A1 position and all three hydrogen atoms lie in the basal B positions. In (d), the V_{Zn}-Ga_{Zn}_B1_3H2B1A defect complex is represented, where the Ga_{Zn} lies in the basal B1 position, two hydrogen atoms lie in the basal B positions, and one hydrogen atom lies in the axial A position. Large grey balls, small red balls, and large green balls denote Zn, O, and Ga atoms, respectively. Small white balls are hydrogen atoms. The Zn atom in front of the V_{Zn} was taken out for the sake of clarity and only its bonds with the neighboring O atoms are represented.

Figure 5a shows the simulated XANES spectra for the four different position of the V_{Zn} using the relaxed structural models denoted as V_{Zn}-Ga_{Zn}_B1, V_{Zn}-Ga_{Zn}_B2, V_{Zn}-Ga_{Zn}_A1, and V_{Zn}-Ga_{Zn}_A2. For the sake of simplicity, the simulated XLD spectra were convoluted with only the Ga core-hole lifetime. Although the presence of V_{Zn} does not affect the overall shape of the XLD spectra, important differences occur at the beginning of the spectra, i.e. just above the Fermi level with the first negative peak marked by * in **Figure 5a**. This makes the comparison between the different spectra possible. The fact that the overall

shape of the XLD spectra remains similar is related to the fact that the introduction of V_{Zn} keeps the wurtzite structure unchanged and the lattice parameter after relaxation of the cell is within 0.01Å similar to the pristine one. It should be emphasized that most of the differences arise from the V_{Zn} and are not due to the change of the averaged nearest-neighbor interatomic distance. The small structural modification as well as the change in the *u*-parameter (within ±1%) have an insignificant influence on the shape of the XLD spectra. Furthermore, the electronic state of the Ga dopants remains Ga^{2+}. The largest change on the XLD spectrum is seen when the V_{Zn} is located in an axial A position, either A1 or A2. In particular, the first negative peak located at 10380 eV in the simulated XLD spectrum for V_{Zn}-Ga_{Zn}_A1 is hardly present in the experimental XLD spectrum, whereas the intensity ratio between the peaks located at 10383 and 10391 eV is completely different for V_{Zn}-Ga_{Zn}_A2. For the cases where the V_{Zn} lies in the basal B position, the modifications in the XLD spectra are less pronounced since the XANES spectra are averaged over the *a* and *b*-basal planes in order to be compliant with the experimental measurements. When the V_{Zn} is placed in the second coordination shell (i.e. V_{Zn}-Ga_{Zn}_B2) or even further, only minor differences are observed as compared with the XLD spectrum simulated without V_{Zn} (i.e. Ga_{Zn}). As a result, for the cases of V_{Zn}-Ga_{Zn}_B1, V_{Zn}-Ga_{Zn}_B2 and Ga_{Zn}, the intensity of the negative shoulder on the peak located at 10380 eV (marked with an asterisk in **Figure 5a**) is less intense only for V_{Zn}-Ga_{Zn}_B1, and therefore it reproduces better the experimental XLD spectrum as shown in **Figure 2b** especially in the low energy part. Based on a linear combination of the XLD spectra of those three defects, it appears that the amount of V_{Zn}-Ga_{Zn}_B1 must be the largest one. As an intermediate conclusion, V_{Zn} should be located in the first coordination shell and preferentially lie in the basal B1 position.

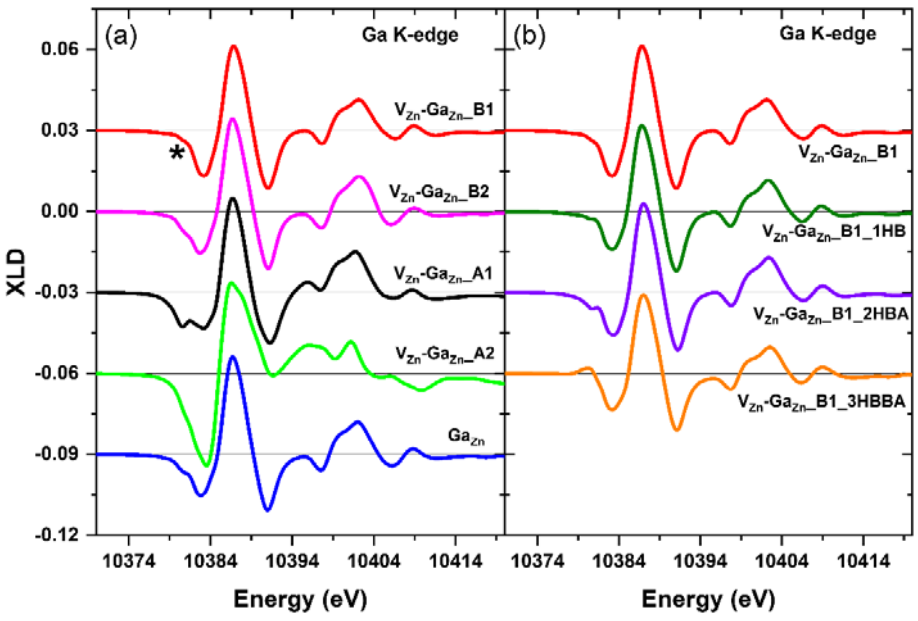

Figure 5. (a) Simulated XLD spectra for various relaxed structural models combining one V_{Zn} in axial A1/A2 or B1/B2 positions with one Ga_{Zn} as V_{Zn}-Ga_{Zn} defect complexes. (b) Simulated XLD spectra for various relaxed structural models combining one V_{Zn} in basal B1 position with one Ga_{Zn} and the presence of one, two or three hydrogen atoms close to the V_{Zn} in axial A and/or basal B positions as V_{Zn}-Ga_{Zn}-*n*H defect complexes. The A1 and B1 nomenclature stands for the first coordination shell in the axial and basal positions, respectively, while the A2 and B2 nomenclature stands for the second coordination shell in the axial and basal positions, respectively. All spectra are convoluted with only the Ga core-hole lifetime.

In addition, the simulated XLD spectra related to V_{Zn}-Ga_{Zn}_B1 with the presence of one, two or three hydrogen atoms close to the V_{Zn} are considered. In the DFT calculations, those atoms are used in order to saturate the O dangling bonds and hence, the distinct basal or axial hydrogen positions are considered, e.g. V_{Zn}-Ga_{Zn}_B1_2HBB, for 2 hydrogen atoms - both in basal positions - V_{Zn}-Ga_{Zn}_B1_2HBA, for 2 hydrogen atoms - one in basal and one in axial position. It should be noted that when the charge is not denoted, the defect complex is considered as neutral. **Figure 5b** shows the simulated XLD spectra for various relaxed structural models combining one single V_{Zn} in the basal position in the first coordination shell (B1) with one Ga_{Zn} and the presence of one, two or three hydrogen atoms close to the V_{Zn}. We can see that by adding a single hydrogen atom to V_{Zn}-Ga_{Zn}_B1 , the agreement with the experimental XLD spectrum is further improved in the low energy part. The negative shoulder on the peak located at 10380 eV is rather well suppressed, allowing us to conclude that V_{Zn}-Ga_{Zn}_B1_1HB is most certainly the dominant defect complex formed. However, we cannot exclude that either all three defect complexes with one, two or three hydrogen atoms or the ones with two and three hydrogen atoms, could be more or less equally present. Indeed, the shoulder at the low energy part of the XLD spectrum is opposite in sign for V_{Zn}-Ga_{Zn}_B1_2HBA and V_{Zn}-Ga_{Zn}_B1_3HBBA, hence their average is very close to V_{Zn}-Ga_{Zn}_B1_1HB and therefore may also be compatible with the experimental XLD spectrum. However, if one considers them individually, the simulated XLD spectrum for V_{Zn}-Ga_{Zn}_B1_1HB is the closest to the experimental one as plotted in **Figure 2b**. It is worth noticing that such investigation of hydrogen-based defect complexes is not possible when using EXAFS, since this technique is not sensitive to hydrogen bonds contrary to XLD.

The formation energies of the V_{Zn}-Ga_{Zn}-*n*H defect complexes as a function of the Fermi level are presented in **Figure 6a-b** for Zn- and O-rich conditions, respectively. The study on the interaction between two V_{Zn} and one Ga_{Zn} concluded in two models presented in Supplementary material [64]. The comparison of their formation energies reveals that the model presented in [64] of Supplemental material is the favorable one. However, as seen in **Figure 6a-b,** the $2V_{Zn}$-Ga_{Zn} defect complex is energetically unfavorable with respect to the rest of the investigated structural models except for O-rich conditions with the Fermi level close to the CBM for which the required formation energy excess is less. The $2Ga_{Zn}$-V_{Zn} defect complex is not taken into consideration in the present DFT and XLD simulations owing to the fact that V_{Zn} are more

mobile thanks to their lower formation energy and smaller activation energy for diffusion than Ga dopants in ZnO. Consequently, they can much more easily form V_{Zn} clusters. Ga dopants in ZnO are more likely to be immobile or exhibit limited mobility, especially at low doping concentrations and low temperatures, due to their larger size and higher activation energy for diffusion [65]. Recently, it has been denoted that the formation of the ($2Ga_{Zn}$-V_{Zn}) defect complex is challenging due to the need for Ga dopants to diffuse. The Ga dopant diffusion is slower than the Zn self-diffusion because of the low impurity to host-cation ratio [66].

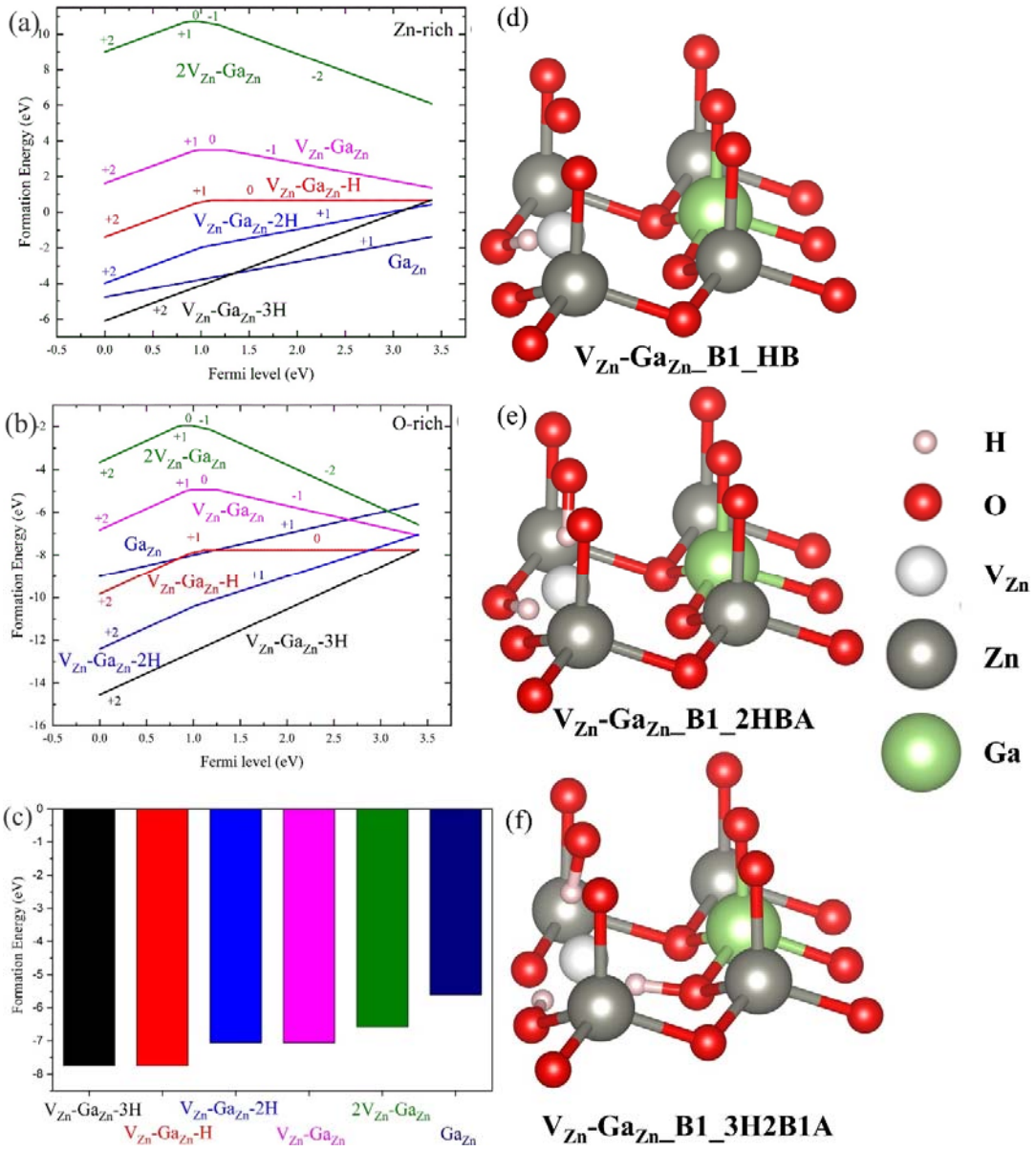

Figure 6. Formation energies of Ga- and hydrogen-related defects in ZnO as a function of Fermi level determined by DFT calculations for (a) Zn- and (b) O-rich conditions. The most stable atomic configuration with the lowest energy is presented for each charge state. The zero of Fermi energy was set at the VBM. The chemical potential values of $\mu_O = -4.22$ eV (Zn-rich), $\mu_O = 0$ eV (O-rich), and $\mu_H = -0.475$ eV were used. (c) Formation energies of the different Ga- and hydrogen-related defects for O-rich conditions considering the Fermi level close to the CBM. (d-f) Relaxed structural models for the most stable atomistic configurations of the V_{Zn}-Ga_{Zn}-*n*H related defect complexes having the Ga dopant in basal position with respect to the V_{Zn}. In (d), the basal V_{Zn}-Ga_{Zn}_B1_HB defect complex is given with one hydrogen atom saturating an oxygen dangling bond in basal position. In (e), the V_{Zn}-Ga_{Zn}_B1_2HBA defect complex is provided with two hydrogens, one in basal position and one in axial position. In (f), the V_{Zn}-Ga_{Zn}_B1_3H2B1A defect complex is given with three hydrogens, two hydrogens in basal and one in axial position. Large grey balls, small red balls, and large green balls denote Zn, O, and Ga atoms, respectively. Small ping balls are hydrogen atoms. For the sake of clarity, the position of the V_{Zn} is represented with a white ball.

For Zn-rich conditions with the Fermi level close to the CBM, Ga_{Zn} has the lowest formation energy and acts as a shallow donor. The V_{Zn}-Ga_{Zn}-3H defect complex with a +2 charge state as a shallow donor as well is energetically favorable only when the Fermi level is close to the VBM. The rest of the defect complexes related to V_{Zn} and Ga_{Zn} requires an energy excess of more than 1.5 eV to be formed. Interestingly, it should be noted that starting from Zn- towards O-rich conditions, the formation energies of defect complexes related to V_{Zn} and Ga_{Zn} are lowered with respect to the formation energy of single Ga_{Zn}. Importantly, intermediate and O-rich conditions should be considered during the CBD of ZnO NWs [67]. In particular, the need for placing the CBD of ZnO NWs in a high pH-region to efficiently incorporate Ga dopants using attractive electrostatic forces in the chemical bath corresponds to more oxidizing and hence O-rich conditions [31]. For O-rich conditions with the Fermi level close to the CBM as expected for ZnO NWs grown by CBD [67], all the defects and defect complexes related to V_{Zn} and Ga_{Zn} are energetically favorable, as seen in **Figure 6c**. The V_{Zn}-Ga_{Zn} defect complex with a –1 charge state acting as a deep acceptor is specifically more favorable energetically than single Ga_{Zn} as reported in Ref.[34]. However, the hydrogen passivated V_{Zn}-Ga_{Zn} defect complexes (V_{Zn}-Ga_{Zn}-*n*H) in the form of V_{Zn}-Ga_{Zn}-H, V_{Zn}-Ga_{Zn}-2H, and V_{Zn}-Ga_{Zn}-3H as represented in **Figure 6d-f** should be considered by far dominant even with the Fermi level in the middle of the band gap. Here, V_{Zn}-Ga_{Zn}-H with a zero charge state acting as a neutral complex and V_{Zn}-Ga_{Zn}-3H with a +2 charge state acting as a doubly ionized shallow donor have the lowest formation energy. In contrast, the formation energy of V_{Zn}-Ga_{Zn}-2H with a +1 charge state acting as a singly ionized shallow donor is slightly higher. In other words, the family of V_{Zn}-Ga_{Zn}-*n*H defect complexes overall provides a large amount of free electrons to Ga-doped ZnO NWs grown by CBD and thus accounts for their high electrical conductivity with a free electron density ranging from 3.10×10^{18} to 9.00×10^{19} cm^{-3} as measured by scanning spreading resistance microscopy in Ref.[68]. This mainly originates from the massive incorporation of V_{Zn}-Ga_{Zn}-2H and V_{Zn}-Ga_{Zn}-3H defect complexes. The V_{Zn}-Ga_{Zn}-H defect complex

is instead electrically inactive despite its high concentration, meaning that the incorporation of hydrogen and Ga dopants during the CBD of ZnO NWs is of the same order of magnitude. Hydrogen acts as an efficient passivating species even when an intentional dopant is used during the CBD process. These findings show that the residual and intentional doping processes are highly correlated and that any optimization of the optical and electrical properties of ZnO NWs grown by CBD should take into account significant interplay effects between the hydrogen and intentional dopants.

CONCLUSIONS

In summary, the XLD spectra of Ga-doped ZnO NWs grown by CBD using synchrotron-based X-ray radiation coupled with DFT calculations reveal that the family of V_{Zn}-Ga_{Zn}-*n*H defect complexes is predominantly formed. The V_{Zn}-Ga_{Zn}-2H and V_{Zn}-Ga_{Zn}-3H defect complexes acting as two singly and doubly shallow donors, respectively, accounts for the high electrical conductivity of Ga-doped ZnO NWs although the V_{Zn}-Ga_{Zn}-H defect complex as a neutral complex present the highest concentration. These findings revisit the nature of intentional dopant-induced defects and defect complexes in ZnO NWs grown by CBD. They further emphasize that the residual and intentional doping processes are high correlated through significant interplay effects. Hydrogen is found to act as an efficient passivating species, even for intentional dopants like Ga. Eventually, hydrogen should be taken into account in unintentionally doped ZnO NWs grown by CBD as major defects for tuning their optical and electrical properties, but also in intentionally doped ZnO NWs through its efficient passivating effect.

ACKNOWLEDGMENTS

The authors thank Odette Chaix-Pluchery, Isabelle Gélard, and Laetitia Rapenne from LMGP, Grenoble, France, for their assistance in Raman scattering and EDS measurements, respectively. The authors warmly thank Yves Joly from Institut Néel, Grenoble, France, for implementing the exchange-correlation potential PBE96 in the FDMNES code. The authors acknowledge the financial support by the French National Research Agency through the projects DOSETTE (ANR-17-CE24-0004) and ROLLER (ANR-17-CE09-0033). P.G. was supported by a doctoral fellowship from the CDP Eco-SESA (ANR-15-IDEX-02). The authors further acknowledge ESRF synchrotron for the provision of beamtime and the facilities, and the scientific and technical assistance of CMTC characterization platform of Grenoble INP, which is supported by the Centre of Excellence of Multifunctional Architectured Materials (LabEx CEMAM) under the contract ANR-10-LABX-44-01 funded by the "Investments for the Future" Program. This research further benefited from CIMENT/GRICAD platform in Grenoble for computational resources as well as by computational time granted from Greek Research & Technology Network (GRNET) in 'ARIS' National HPC infrastructure under the project NOUS (pr012041).

REFERENCES

[1] L. Vayssieres, K. Keis, S. E. Lindquist, and A. Hagfeldt, J. Phys. Chem. B **105**, 3350 (2001).
[2] L. Vayssieres, Adv. Mater. **15**, 464 (2003).
[3] D. Vanmaekelbergh and L. K. van Vugt, Nanoscale **3**, 2783 (2011).
[4] R. Faiz, Optical Engineering **58**, 010901 (2019).
[5] W. Ouyang, J. Chen, Z. Shi, and X. Fang, Appl. Phys. Rev. **8**, 031315 (2021).
[6] V. Consonni, J. Briscoe, E. Karber, X. Li, and T. Cossuet, Nanotechnology **30**, 41, 362001 (2019).
[7] J. Briscoe and S. Dunn, Nano Energy **14**, 15 (2015).
[8] J. Liu, Y. Wang, J. Ma, Y. Peng, and A. Wang, Journal of Alloys and Compounds **783**, 898 (2019).
[9] A. Mirzaei, J.-H. Lee, S. M. Majhi, M. Weber, M. Bechelany, H. W. Kim, and S. S. Kim, J. Appl. Phys. **126**, 241102 (2019).
[10] D. Lincot, MRS Bull. **35**, 778 (2010).
[11] S. Xu and Z. L. Wang, Nano Res. **4**, 1013 (2011).
[12] A. Janotti and C. G. Van de Walle, Rep. Prog. Phys. **72**, 29, 126501 (2009).
[13] M. D. McCluskey and S. J. Jokela, J. Appl. Phys. **106**, 13, 071101 (2009).
[14] F. Tuomisto, V. Ranki, K. Saarinen, and D. C. Look, Phys. Rev. Lett. **91**, 205502 (2003).
[15] A. Janotti and C. G. Van de Walle, Phys. Rev. B **76**, 22, 165202 (2007).
[16] X. J. Wang, L. S. Vlasenko, S. J. Pearton, W. M. Chen, and I. A. Buyanova, Journal of Physics D: Applied Physics **42**, 175411 (2009).
[17] C. G. Van de Walle, Phys. Rev. Lett. **85**, 1012 (2000).
[18] A. Janotti and C. G. Van de Walle, Nat. Mater. **6**, 44 (2007).
[19] D. M. Hofmann, A. Hofstaetter, F. Leiter, H. J. Zhou, F. Henecker, B. K. Meyer, S. B. Orlinskii, J. Schmidt, and P. G. Baranov, Phys. Rev. Lett. **88**, 4, 045504 (2002).
[20] J. L. Lyons, J. B. Varley, D. Steiauf, A. Janotti, and C. G. Van de Walle, J. Appl. Phys. **122**, 12, 035704 (2017).
[21] Y. K. Frodason, K. M. Johansen, T. S. Bjorheim, B. G. Svensson, and A. Alkauskas, Phys. Rev. B **97**, 8, 104109 (2018).
[22] J. Villafuerte, F. Donatini, J. Kioseoglou, E. Sarigiannidou, O. Chaix-Pluchery, J. Pernot, and V. Consonni, The Journal of Physical Chemistry C (2020).
[23] X. N. Li, B. Keyes, S. Asher, S. B. Zhang, S. H. Wei, T. J. Coutts, S. Limpijumnong, and C. G. Van de Walle, Appl. Phys. Lett. **86**, 3, 122107 (2005).
[24] S. J. Jokela and M. D. McCluskey, Phys. Rev. B **76**, 4, 193201 (2007).
[25] M. N. Amini, R. Saniz, D. Lamoen, and B. Partoens, Phys. Chem. Chem. Phys. **17**, 5485 (2015).
[26] D. Y. Yong, H. Y. He, Z. K. Tang, S. H. Wei, and B. C. Pan, Phys. Rev. B **92**, 5, 235207 (2015).
[27] J. Villafuerte, O. Chaix-Pluchery, J. Kioseoglou, F. Donatini, E. Sarigiannidou, J. Pernot, and V. Consonni, Phys. Rev. Mater. **5**, 056001 (2021).
[28] X. H. Huang, Z. Y. Zhan, K. P. Pramoda, C. Zhang, L. X. Zheng, and S. J. Chua, Crystengcomm **14**, 5163 (2012).
[29] E. G. Barbagiovanni, R. Reitano, G. Franzo, V. Strano, A. Terrasi, and S. Mirabella, Nanoscale **8**, 995 (2016).
[30] C. Verrier, E. Appert, O. Chaix-Pluchery, L. Rapenne, Q. Rafhay, A. Kaminski-Cachopo, and V. Consonni, Inorg. Chem. **56**, 13111 (2017).

[31] P. Gaffuri, E. Appert, O. Chaix-Pluchery, L. Rapenne, M. Salaun, and V. Consonni, Inorg. Chem. **58**, 10269 (2019).
[32] C. Lausecker, B. Salem, X. Baillin, O. Chaix-Pluchery, H. Roussel, S. Labau, B. Pelissier, E. Appert, and V. Consonni, Inorg. Chem. **60**, 1612 (2021).
[33] F. Wang *et al.*, Nanotechnology **22**, 225602 (2011).
[34] D. O. Demchenko, B. Earles, H. Y. Liu, V. Avrutin, N. Izyumskaya, Ü. Özgür, and H. Morkoç, Phys. Rev. B **84**, 075201 (2011).
[35] H. Wang, S. Baek, J. Song, J. Lee, and S. Lim, Nanotechnology **19**, 075607 (2008).
[36] A. Escobedo-Morales and U. Pal, Appl. Phys. Lett. **93**, 193120 (2008).
[37] G. Pineda-Hernández, A. Escobedo-Morales, U. Pal, and E. Chigo-Anota, Mater. Chem. Phys. **135**, 810 (2012).
[38] G. C. Park, S. M. Hwang, J. H. Lim, and J. Joo, Nanoscale **6**, 1840 (2014).
[39] R. Li, C. Yu, H. Dong, W. Jia, T. Li, Z. Zhang, and B. Xu, RSC Adv. **7**, 49613 (2017).
[40] G. Ciatto, A. Di Trolio, E. Fonda, P. Alippi, A. M. Testa, and A. A. Bonapasta, Phys. Rev. Lett. **107**, 127206 (2011).
[41] Q. Ma, J. T. Prater, C. Sudakar, R. A. Rosenberg, and J. Narayan, Journal of Physics: Condensed Matter **24**, 306002 (2012).
[42] E. Sarigiannidou, F. Wilhelm, E. Monroy, R. M. Galera, E. Bellet-Amalric, A. Rogalev, J. Goulon, J. Cibert, and H. Mariette, Phys. Rev. B **74**, 041306 (2006).
[43] A. Ney, K. Ollefs, S. Ye, T. Kammermeier, V. Ney, T. C. Kaspar, S. A. Chambers, F. Wilhelm, and A. Rogalev, Phys. Rev. Lett. **100**, 157201 (2008).
[44] A. Rogalev and F. Wilhelm, The Physics of Metals and Metallography **116**, 1285 (2015).
[45] O. Bunău and Y. Joly, Journal of Physics: Condensed Matter **21**, 345501 (2009).
[46] S. A. Guda *et al.*, Journal of Chemical Theory and Computation **11**, 4512 (2015).
[47] G. Kresse and J. Furthmüller, Phys. Rev. B **54**, 11169 (1996).
[48] G. Kresse and D. Joubert, Phys. Rev. B **59**, 1758 (1999).
[49] P. E. Blochl, Phys. Rev. B **50**, 17953 (1994).
[50] J. P. Perdew, K. Burke, and M. Ernzerhof, Phys. Rev. Lett. **77**, 3865 (1996).
[51] J. P. Perdew, K. Burke, and M. Ernzerhof, Phys. Rev. Lett. **78**, 1396 (1997).
[52] S. L. Dudarev, G. A. Botton, S. Y. Savrasov, C. J. Humphreys, and A. P. Sutton, Phys. Rev. B **57**, 1505 (1998).
[53] P. Erhart, K. Albe, and A. Klein, Phys. Rev. B **73**, 9, 205203 (2006).
[54] N. N. Lathiotakis, A. N. Andriotis, and M. Menon, Phys. Rev. B **78**, 4, 193311 (2008).
[55] R. M. Sheetz, I. Ponomareva, E. Richter, A. N. Andriotis, and M. Menon, Phys. Rev. B **80**, 4, 195314 (2009).
[56] Q. B. Wang, C. Zhou, J. Wu, and T. Lu, Opt. Commun. **297**, 79 (2013).
[57] L. Dong, R. Jia, B. Xin, B. Peng, and Y. Zhang, Scientific Reports **7**, 40160 (2017).
[58] J. L. Lyons, A. Janotti, and C. G. Van de Walle, Phys. Rev. B **80**, 205113 (2009).
[59] C. Freysoldt, B. Grabowski, T. Hickel, J. Neugebauer, G. Kresse, A. Janotti, and C. G. Van de Walle, Rev. Mod. Phys. **86**, 253 (2014).
[60] G.-Y. Huang, C.-Y. Wang, and J.-T. Wang, Physica B: Condensed Matter **405**, 158 (2010).
[61] H. F. McMurdie, M. C. Morris, E. H. Evans, B. Paretzkin, W. Wong-Ng, L. Ettlinger, and C. R. Hubbard, Powder Diffraction **1**, 64 (2013).
[62] H. Karzel *et al.*, Phys. Rev. B **53**, 11425 (1996).
[63] A. Ney, V. Ney, K. Ollefs, D. Schauries, F. Wilhelm, and A. Rogalev, Journal of Surfaces and Interfaces of Materials **2**, 14 (2014).
[64] See Supplemental Material at [URL will be inserted by publisher] for Zn and Ga K-edges XANES spectra as measured with total fluorescence yield and shown in Figure SM1. In Figure SM2 (a), both

vacancies and the Ga substitutional atom are in the same basal plane, while the Ga atom is between vacancies. In Figure SM2 (b), in comparison with the previous model one vacancy is located on the upper layer and hence they are not in the same basal plane. Large grey balls, small red balls, and large green balls denote zinc, oxygen, and gallium atoms, respectively. The energetical favorable is the one in Figure SM2 (a).

[65] D. Steiauf, J. L. Lyons, A. Janotti, and C. G. Van de Walle, APL Mater. **2**, 096101 (2014).

[66] Y. Ke, S. Lany, J. J. Berry, J. D. Perkins, P. A. Parilla, A. Zakutayev, T. Ohno, R. O'Hayre, and D. S. Ginley, Adv. Funct. Mater. **24**, 2875 (2014).

[67] J. Villafuerte, E. Sarigiannidou, F. Donatini, J. Kioseoglou, O. Chaix-Pluchery, J. Pernot, and V. Consonni, Nanoscale Advances **4**, 1793 (2022).

[68] O. Synhaivskyi, D. Albertini, P. Gaffuri, J.-M. Chauveau, V. Consonni, B. Gautier, and G. Bremond, The Journal of Physical Chemistry C **125**, 15373 (2021).